frontiers | Frontiers in Physics

ORIGINAL RESEARCH
published: 12 May 2022
doi: 10.3389/fphy.2022.880793

Fragmentation Dynamics of Fluorene Explored Using Ultrafast XUV-Vis Pump-Probe Spectroscopy

*D. Garg[1,2†], J. W. L. Lee[1,3†], D. S. Tikhonov[1,4†], P. Chopra[1,4], A. L. Steber[1,4,5], A. K. Lemmens[6,7], B. Erk[1], F. Allum[3], R. Boll[8], X. Cheng[1,9], S. Düsterer[1], S. Gruet[1], L. He[9], D. Heathcote[3], M. Johny[2,5,9], M. M. Kazemi[1], H. Köckert[3], J. Lahl[10], D. Loru[1,4], S. Maclot[10,11], R. Mason[3], E. Müller[1], T. Mullins[9], P. Olshin[12], C. Passow[1], J. Peschel[10], D. Ramm[1], D. Rompotis[1,8], S. Trippel[5,9], J. Wiese[9,13], F. Ziaee[14], S. Bari[1], M. Burt[3], J. Küpper[2,5,9,13], A. M. Rijs[15], D. Rolles[14], S. Techert[1,16], P. Eng-Johnsson[10], M. Brouard[3], C. Vallance[3], B. Manschwetus[1] and M. Schnell[1,4]**

[1]Deutsches Elektronen-Synchrotron DESY, Hamburg, Germany, [2]Department of Physics, Universität Hamburg, Hamburg, Germany, [3]Chemistry Research Laboratory, Department of Chemistry, University of Oxford, Oxford, United Kingdom, [4]Institute of Physical Chemistry, Christian-Albrechts-Universität zu Kiel, Kiel, Germany, [5]Center for Ultrafast Imaging, Universität Hamburg, Hamburg, Germany, [6]Van't Hoff Institute for Molecular Sciences, University of Amsterdam, Amsterdam, Netherlands, [7]FELIX Laboratory, Radboud University, Nijmegen, Netherlands, [8]European XFEL, Schenefeld, Germany, [9]Center for Free-Electron Laser Science, Deutsches Elektronen-Synchrotron DESY, Hamburg, Germany, [10]Department of Physics, Lund University Lund, Sweden, [11]Physics Department, University of Gothenburg, Gothenburg, Sweden, [12]Department of Chemistry, College of Natural Sciences, Ulsan National Institute of Science and Technology, Ulsan, South Korea, [13]Department of Chemistry, Universität Hamburg, Hamburg, Germany, [14]J. R. Macdonald Laboratory, Department of Physics, Kansas State University, Manhattan, KS, United States, [15]Division of BioAnalytical Chemistry, Vrije Universiteit Amsterdam, Amsterdam, Netherlands, [16]Institute for X-Ray Physics, Georg-August-Universität, Göttingen, Germany

OPEN ACCESS

Edited by:
Yuichi Fujimura,
Tohoku University, Japan

Reviewed by:
Nigel John Mason,
University of Kent, United Kingdom
Aparna Shastri,
Bhabha Atomic Research Centre (BARC), India

***Correspondence:**
M. Schnell
melanie.schnell@desy.de

[†]These authors have contributed equally to this work and share first authorship

Specialty section:
This article was submitted to Physical Chemistry and Chemical Physics, a section of the journal Frontiers in Physics

Received: 21 February 2022
Accepted: 27 April 2022
Published: 12 May 2022

Citation:
Garg D, Lee JL, Tikhonov DS, Chopra P, Steber AL, Lemmens AK, Erk B, Allum F, Boll R, Cheng X, Düsterer S, Gruet S, He L, Heathcote D, Johny M, Kazemi MM, Köckert H, Lahl J, Loru D, Maclot S, Mason R, Müller E, Mullins T, Olshin P, Passow C, Peschel J, Ramm D, Rompotis D, Trippel S, Wiese J, Ziaee F, Bari S, Burt M, Küpper J, Rijs AM, Rolles D, Techert S, Eng-Johnsson P, Brouard M, Vallance C, Manschwetus B and Schnell M (2022) Fragmentation Dynamics of Fluorene Explored Using Ultrafast XUV-Vis Pump-Probe Spectroscopy. Front. Phys. 10:880793. doi: 10.3389/fphy.2022.880793

We report on the use of extreme ultraviolet (XUV, 30.3 nm) radiation from the Free-electron LASer in Hamburg (FLASH) and visible (Vis, 405 nm) photons from an optical laser to investigate the relaxation and fragmentation dynamics of fluorene ions. The ultrashort laser pulses allow to resolve the molecular processes occurring on the femtosecond timescales. Fluorene is a prototypical small polycyclic aromatic hydrocarbon (PAH). Through their infrared emission signature, PAHs have been shown to be ubiquitous in the universe, and they are assumed to play an important role in the chemistry of the interstellar medium. Our experiments track the ionization and dissociative ionization products of fluorene through time-of-flight mass spectrometry and velocity-map imaging. Multiple processes involved in the formation of each of the fragment ions are disentangled through analysis of the ion images. The relaxation lifetimes of the excited fluorene monocation and dication obtained through the fragment formation channels are reported to be in the range of a few tens of femtoseconds to a few picoseconds.

Keywords: polycyclic aromatic hydrocarbon (PAH), time-resolved spectroscopy, velocity-map imaging mass spectrometry, ultrafast dynamics of molecules, free electron laser

1 INTRODUCTION

The rich molecular inventory of the interstellar medium (ISM) includes polycyclic aromatic hydrocarbons (PAHs), which are estimated to constitute more than 10% of the total galactic carbon [1–4]. UV photons present in the ISM can be absorbed by the PAHs, which can lead to photodissociation, photoionization, photoemission, and photoelectron emission [5]. PAH molecules

absorb UV photons, and they relax through IR photon emission [6]. PAHs also play an active role in the ISM through the photoelectric effect where the photoelectrons emitted from the PAH provide the energy to the gas and atoms in the ISM. It also has been suggested that near the photodissociation regions (PDRs), photolysis of these PAHs may lead to the formation of small hydrocarbons [3, 5]. The unidentified infrared bands (UIR), measured in the interstellar atomic hydrogen (H II) and planetary nebula regions of the ISM, are attributed to PAHs and their clusters in cationic or neutral form [5, 7–9] and are also referred to as Aromatic Infrared Bands (AIBs). With radio telescope observations, the support of laboratory experiments, and quantum chemical calculations, the first PAH (indene) and substituted PAHs (1-cyano-naphthalene and 2-cyano-naphthalene) have recently been identified in the ISM [10–12]. To understand the formation of these species, various mechanisms and hypotheses are proposed, involving small hydrocarbons or hydrogen as precursors. These small species might become available as the fragmentation products of other PAHs under harsh radiations [12–14]. Understanding the complex pathways leading to the formation of the detected carbon-containing species extending from small-sized PAHs to large carbonaceous species (e.g., C_{60}^{+} [15]) will provide guidance towards finding more molecules and exploring the constituents of the ISM in the presence of photons, ions, and electrons. One of the ways to look into the complex chemical reactions involved in the ISM is to study the interaction of the relevant molecules with radiation at well defined wavelengths and observing the dissociation products to provide insights into the possible species present in the ISM. Knowledge of the reaction products and the average relaxation lifetimes of the excited species will aid astrochemical evolution models [11].

Despite the remarkable stability of PAHs, they can undergo ionization, isomerization, fragmentation, and dissociative ionization when exposed to high-energy radiation [16–21]. Understanding these processes is challenging for both computational and experimental methods because a large number of nuclear and electronic degrees of freedom are strongly coupled when the system is highly excited and typically enters the non-adiabatic regime, in which the Born-Oppenheimer approximation breaks down [22–25]. The excited species then relax on ultrafast timescales, which can be investigated by pump-probe spectroscopy. Such ultrafast timescales have been observed and reported by several previous laboratory studies [16, 18, 21, 26].

Different experimental approaches exist to investigate the fragmentation products and the fragmentation dynamics of PAHs within different energy regimes (XUV, UV, Vis, IR) [16, 17, 20, 27–29]. The general fragmentation pattern after the interaction of these molecules with high energy photons (a few 10 eV) shows multiple hydrogen losses and a prominent carbon backbone fragmentation, which majorly involves an even number of carbon atoms, for example in the form of acetylene units. The interaction of the molecular beam with high energy photons may also lead to double ionization of the parent molecules, which then dissociate into two monocations involving the loss of zero or an even number of carbon atoms, as shown in photoelectron-photoion-photoion-coincidence (PEPIPICO) measurements [30, 31]. In a recent study employing recoil-frame covariance analysis of velocity-map imaging, we observed a similar behaviour [16]. In the ultraviolet regime, larger PAHs (more than 32 carbon atoms) show more dehydrogenation and less carbon-carbon fragmentation [5] than the small and medium-sized PAHs, which undergo fragmentation affecting the carbon skeleton. Fragmentation of the carbon skeleton could also provide information on the origin of potential species for the hydrogen abstraction and acetylene addition (HACA) model, which is widely suggested as a possible PAH growth mechanism in the photosphere of the asymptotic giant branch stars, where small hydrocarbons form large molecules and soot analogues in the ISM [5, 32].

Here, we present the results from an XUV-Vis pump-probe spectroscopy experiment on the PAH fluorene (FLU, $C_{13}H_{10}$, molecular mass = 166 a.m.u.), which contains two aliphatic hydrogen atoms. The fluorenyl cation, which is dehydrogenated singly ionized FLU, has been reported to be formed from various other PAHs [33–35], which points towards its considerable stability. In a previous study, FLU molecules were irradiated with visible light (593 nm) and their charged clusters were observed to undergo photo-dehydrogenation and photo-isomerization, resulting in the formation of bowl-type structures [36]. This "curling" mechanism was discussed as a bottom-up step to form the fullerene-type structures that are found in the interstellar medium [36]. The formation of stable large FLU clusters is also interesting in the context of the "grandPAH hypothesis," according to which only the most stable species are thought to survive in the photodissociation regions [37]. We investigate the interaction of FLU with XUV radiation centered at 30.3 nm (40.9 eV), which corresponds to the helium (He) II emission line. As the dynamics occur on femtosecond (fs) timescales, we use femtosecond XUV pulses generated from FLASH [38]. The resulting ionized system generated by the XUV radiation is then probed by 405 nm (3.1 eV) visible photons. The studies give insight into the relaxation, dissociation, and ionization dynamics of FLU under XUV conditions.

2 MATERIALS AND METHODS

2.1 Experiments

The experiments were performed using the CFEL-ASG Multi Purpose (CAMP) endstation [39] at the beamline BL1 at the FLASH1 branch of the free-electron laser with a double-sided velocity-map-imaging (VMI) spectrometer installed at the CAMP endstation. We used two pulsed beams (XUV and Vis), operated at a repetition rate of 10 Hz. The XUV pulses (λ = 30.3 nm, pulse duration 80–90 fs (FWHM), which is estimated from the pulse length of electrons [40] using the "LOLA instrument" [41]) were provided by FLASH1 with an average pulse energy of 14.5 μJ, which was then reduced to 1.4 μJ by two aluminium filters of thickness 100.9 nm (55% transmission) and 423.4 nm (28% transmission), and the five beamline mirrors (resultant transmission 62%). The second harmonic generation output of a Ti:Sapphire optical laser, obtained using one beta-barium borate (BBO) crystal, was used as

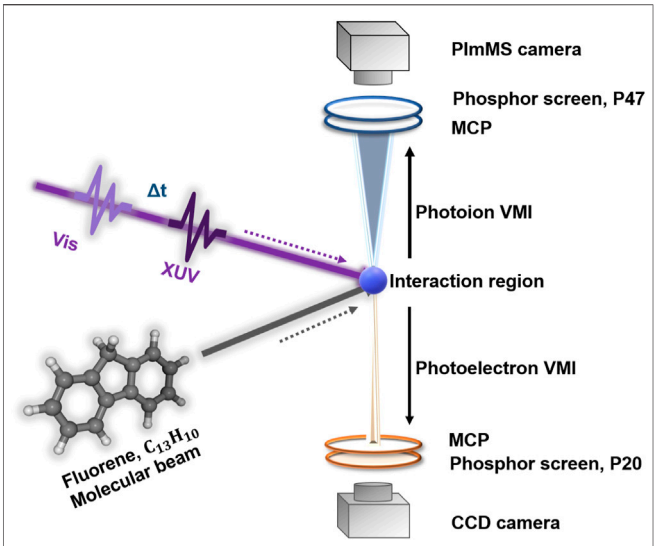

FIGURE 1 | Schematic of the experimental arrangement at the CAMP endstation at FLASH1 (excluding the ion optics for ion and electron extraction) [39]. The supersonically expanded molecular beam interacts with the XUV and Vis pulses (arriving with a delay time, Δt, between them). After interaction, ions and electrons were velocity-mapped on the ion detector assembly (at the top) and on the electron detector assembly (at the bottom). The paths followed by the beams after the interaction are not shown in the figure.

the Vis laser pulse (λ = 405 nm, pulse duration less than ~150 fs, which is estimated from the fundamental beam pulse duration) with a pulse energy up to ~390 μJ [42].

We used the VMI setup [43, 44] at the CAMP endstation [39] to obtain the ion yields and ion momenta of the FLU parent ions (mono-, di-, and trication) as well as fragment ions as a function of pump-probe delay time. FLU was purchased with 98% purity from Sigma-Aldrich and was used without any further purification. A brief description of the experimental procedure and setup (shown in **Figure 1**) is as follows. FLU with a melting point of 116°C was heated to 200°C to produce sufficient molecules in the gas phase. The molecular beam was produced *via* supersonic expansion through a high temperature Even-Lavie pulsed valve with opening times of a few 10 microseconds [45]. We used helium as a carrier gas at 1–2 bar backing pressure. After passing through a pair of skimmers, the well-collimated and internally cooled molecular beam, with the majority of the molecules in their vibrational ground state, entered the vacuum chamber and was irradiated by the two almost collinear beams (XUV and Vis pulses), which crossed each other at a small angle (~1.5°) with different delay times, Δt, between them. The two pulses interact with the neutral molecules perpendicularly. The ions and electrons produced by ionization or dissociative ionization of the neutral molecules were accelerated by an electric field along two diametrically opposed flight tubes and detected at the microchannel plate (MCP) detector/phosphor detector setups in the "top" and "bottom" detector assemblies, respectively. In this work, only the ion data is discussed.

The ion detector assembly consists of a dual MCP detector coupled to a P47 phosphor screen that converts the position information of each ion hit on the detector to light. A multi-mass imaging PImMS2 sensor in a PImMS camera [46, 47] recorded the velocity-mapped 2D ion images formed by the phosphor screen for all the fragments and parent ions in each interaction event. A high-resolution TOF spectrum was obtained by recording the total signal from the MCP using a 2-GHz analog to digital converter (model: ADQ2AC-4G-MTCA, company: SP Devices). Similar to the ion detector assembly, the electrons were simultaneously velocity-mapped onto a P20 phosphor screen and captured by a charged coupled device (CCD) camera. Each experiment involved scanning over the pump-probe delay time between the two laser pulses and recording the ion yield (intensities of the time-of-flight mass spectrum recorded) and ion momenta (extracted from the ion velocity map images) at each step. In this experiment, we scanned a range of 3 picoseconds (ps) of pump-probe delay time with 0.05 ps steps. At each delay value, ~250 measurements were acquired in order to obtain sufficient statistics.

2.2 Analysis

The 2D ion velocity-map images captured from the PImMS camera were fully symmetrized (top/bottom/left/right) and then Abel-inverted to obtain the central slices of the 3D product ion velocity distributions, using the onion peeling method implemented in the PyAbel package available in Python [48, 49]. Angular integration of these Abel-inverted velocity-map ion images generated the radial distribution (in pixels), which was converted to ion momentum using a calibration factor determined through SIMION ion trajectory simulations [50]. The momentum distributions were analyzed as a function of delay time, and the resulting pump-probe delay-time dependent ion yields were fitted using in-house developed open source libraries and scripts [51–53]. The fitting procedure is explained in detail in Refs. [54, 55].

The temporal overlap of the two laser pulses (t_0) was extracted after simultaneously fitting 18 different pump-probe delay time-dependent ion yield curves, which were recorded in the same dataset, and therefore have the same parameter t_0. The resulting t_0 with a fit error of 1 femtosecond was then used as a constraint parameter to fit time-dependent ion yields of other fragments, which were fit with multiple transient features as discussed below for the fragment $C_4H_x^+$. The pump-probe delay time values were corrected for the temporal overlap offset between the two pulses and for jitter in the XUV pulse arrival time that was measured by the beam arrival-time monitor (BAM) [56, 57]. The ion yield intensity was also corrected for shot-to-shot FEL pulse energy fluctuations that is described briefly in the **Supplementary Material**. Covariance analysis [58] was performed on both TOF and VMI results. The TOF measurements enabled us to calculate TOF-TOF partial covariance. The method is explained in detail in Ref. [59], and the results are shared in the **Supplementary Material**. The two-body recoil-frame covariance could be calculated from the VMI data, which are discussed in the results section.

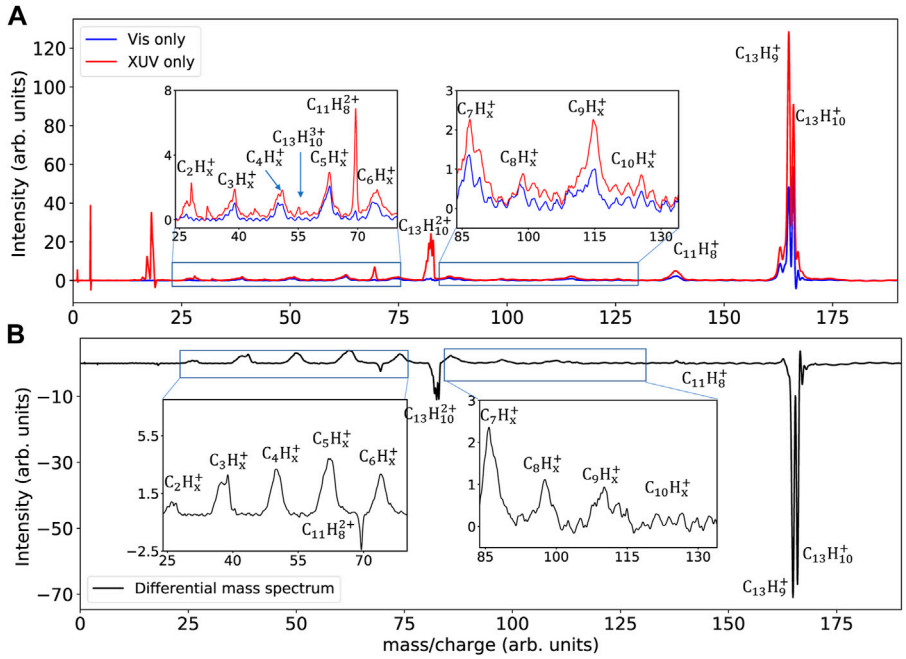

FIGURE 2 | (A) Mass spectra shown for two different conditions: XUV only (red) and Vis only (blue), which were measured using the MCP detector. The insets are the zoomed views of less intense fragments. **(B)** Differential mass spectrum calculated by subtracting the individual XUV only and Vis only spectra from the pump-probe delay-time averaged XUV-Vis mass spectrum in order to visualize the effect of the XUV and Vis pulses.

3 RESULTS

3.1 Time-Independent Results

3.1.1 Ionization and Fragmentation of FLU

Mass spectra obtained after the interaction of FLU with XUV (mass spectrum in red) and Vis (mass spectrum in blue) radiation are shown in **Figure 2A**. Subscript "x" depicts the number of hydrogen atoms attached to the fragments (ranges from 1 to 10). In the following section, we first discuss the effect of Vis and XUV photons on FLU separately before we evaluate their combined effects.

When FLU absorbs Vis photons, mostly single ionization (ionization potential: 7.88 ± 0.05 eV [60]) with loss of up to three hydrogen atoms (hydrogen dissociation energy: ~4 eV [16, 61]) and one acetylene (forming $C_{11}H_x^+$) is observed. The single hydrogen atom loss from FLU^+ is found to be the second most intense peak, FLU^+ being the most intense one. As the energy required for ionization and dissociative ionization is more than the single Vis photon energy (3.1 eV), multi-photon processes must be involved [16]. Consequently, several fragmentation channels are also accessible.

The absorption of XUV photons by FLU leads to single, double, and triple ionization. The singly and doubly charged FLU ions show loss of up to three and four hydrogen atoms, respectively. In the mass spectrum, the intensity of the fluorenyl cation $C_{13}H_9^+$ is observed to be higher than the intensity of $C_{13}H_{10}^+$. The major contribution of $C_{13}H_9^+$ to the mass spectrum can be attributed to the conversion of an sp^3 hybridized carbon to an sp^2 hybridized carbon after loss of an aliphatic hydrogen, which makes the molecule a fully conjugated system. Since a single XUV photon has enough energy to cause ionization and/or hydrogen dissociation, the production of the fluorenyl cation is observed to be more intense during XUV interaction than in the case of Vis pulse interaction that needs multiple photons to produce the fluorenyl cation. Low abundance of the fluorenyl cation is consistent to the observation in other studies with rather low ~4.1 eV photon energy [62] and proton

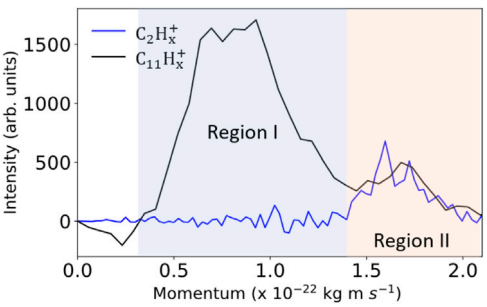

FIGURE 3 | The momentum profiles of $C_2H_x^+$ (blue curve) and $C_{11}H_x^+$ (black curve) fragments are shown for the XUV-only condition and were acquired from the velocity-mapped ion images. Regions I and II mark ions with low and high momentum, respectively. The momentum matches for the two ions, indicating their co-production, which is confirmed by recoil-frame covariance.

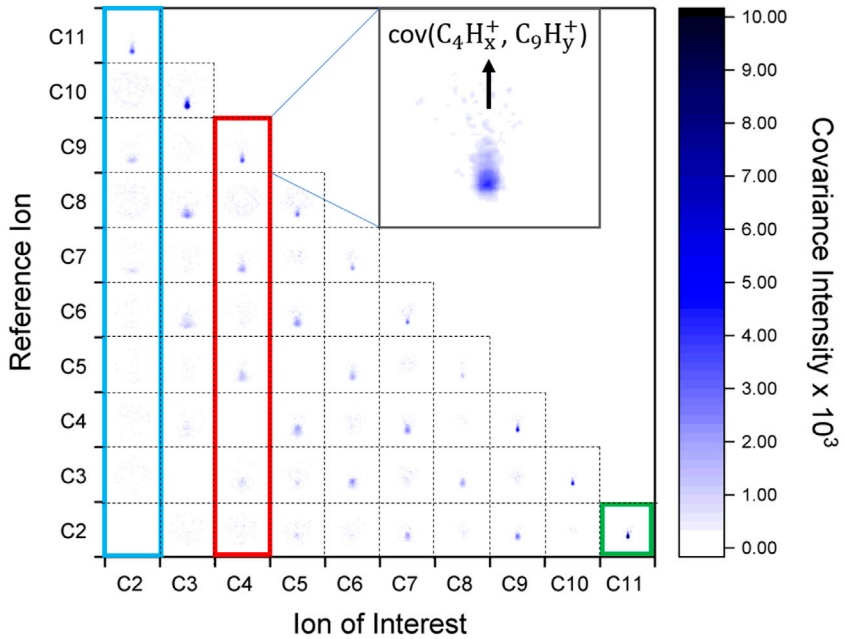

FIGURE 4 | Each square in the dotted grid represents a two-body recoil frame covariance map of the ion of interest with respect to the reference ion, for all the fragment ions, where the direction of the reference ion is vertically upward as also shown in the inset by the black arrow. Self-covariance of an ion with itself is omitted for clarity. Since FLU has 13 carbon atoms, the sum of carbon atoms of the dissociation products cannot exceed 13, and therefore no covariance is expected in the upper half. As an example, the zoomed covariance signal of $C_4H_x^+$ with the reference ion $C_9H_y^+$ is displayed in the inset. The additional subscript "y" depicts the number of hydrogen atoms attached to the fragment, which is the momentum partner of another fragment with the number of hydrogen atoms depicted with subscript "x". The blue rectangle depicts multiple possible ions with which $C_2H_x^+$ could be produced, similarly the red rectangle and green square highlight the possible partners of $C_4H_x^+$ and $C_{11}H_x^+$, respectively.

impact studies [19]. Acetylene loss from the parent monocation forming $C_{11}H_x^+$ and from the parent dication forming $C_{11}H_x^{2+}$ is also observed. The relative abundance of $C_{11}H_x^{2+}$ w.r.t $C_{13}H_x^{2+}$ is higher than that of $C_{11}H_x^+$ w.r.t $C_{13}H_x^+$, which points towards a facilitated acetylene loss from the parent dication than from the parent monocation. The possible dissociation pathways leading to the formation of $C_{11}H_x^+$ and $C_{11}H_x^{2+}$ and the energies involved in dissociation of the parent mono- and dication are summarized in the **Supplementary Material**.

A more prominent $C_2H_x^+$ peak is observed in the XUV-only case compared to the Vis-only condition. During interaction with XUV photons, both the parent monocation and the dication can dissociate to produce $C_2H_x^+$. For the parent monocation, both the formation of the charged acetylene unit, $C_2H_x^+$ (together with the neutral partners, e.g., $C_{11}H_y$, where the subscript "y" depicts the number of hydrogen atoms in this partner fragment), and formation of neutral C_2H_x (together with charged partners, e.g., $C_{11}H_x^+$) are feasible. The parent monocation dissociation will be reflected in the low momentum region, i.e., region I in **Figure 3**, since during the dissociation of the parent monocation, the charged fragments are recoiling from neutral fragments, whereas the parent dication produces $C_2H_x^+$ partnered by charged $C_{11}H_y^+$ resulting in higher momentum and increase the signal measured in region II in **Figure 3**. The co-production of these two fragment ions is indicated by the similar momentum profiles in region II, which is confirmed by the recoil-frame covariance (shown in **Figure 4**). Only a low amount of $C_2H_x^+$ is formed from FLU^+, while significant amounts are formed from the FLU^{2+}.

The differential mass spectrum is calculated by subtracting the individual ion yields observed in the XUV only and the Vis only condition from the XUV-Vis pump-probe delay-time averaged mass spectrum (shown in black in **Figure 2B**). The positive and negative intensity show the increase and decrease in the ion yield, respectively. The decrease in the ion yield of the large fragments or the parent ion species (for example for $C_{13}H_{10}^+$, $C_{13}H_{10}^{2+}$, and $C_{11}H_8^{2+}$) together with the substantial increase in the fragment intensity allude the dissociation of the large species into the smaller fragment ions as a result of the molecular beam interacting with the XUV and Vis pulses.

3.1.2 Ion Momenta and Covariance of Product Fragment Ions

Recoil-frame covariance analysis was performed on the multi-mass VMI data set to discern the correlated ions. The details of covariance mapping can be found in Refs. [63–66]. Briefly, recoil-frame covariance shows the velocity distribution of one ion (ion of interest) with respect to the recoil velocity vector of another ion (reference ion). **Figure 4** shows the covariances between all possible monocation pairs resulting from dissociation of FLU^{2+}. Generally, the intense spot directing opposite to the reference ion direction indicates that the two ions (the ion of interest and the reference ion) are created from the same parent molecule, in a simple two-body decay. Since recoil-frame

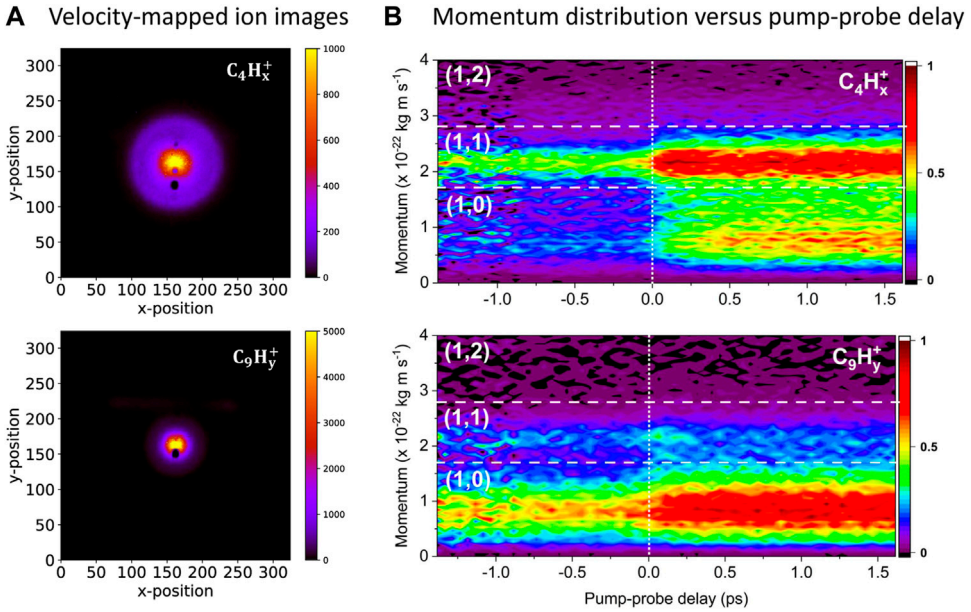

FIGURE 5 | Results for two of the fragments, $C_4H_x^+$ and $C_9H_y^+$: **(A)** 2D raw velocity-mapped ion images for the two fragments. The *x* and *y* axes denote the pixels of the PImMS camera (324 × 324). The black spots in the ion images are due to an artifact in the MCP detector. These images are later fully symmetrized and then Abel-inverted to obtain the central slice of the 3D velocity distribution. This central slice is angularly integrated, and the resultant momentum distribution is plotted as a function of delay time shown in **(B)**. **(B)** Momentum distribution as a function of pump-probe delay for two fragment ions showing momentum matching in the (1,1) channel, indicating their co-production in the same fragmentation reaction, which is verified by the two-body recoil frame covariance. The white vertical dotted line indicates the overlap of the two pulses at t_0.

covariance demonstrates the correlated motion of the two species, the blurred spots indicate that they are produced *via* a more complex mechanism along with other (neutral or charged) partners. It can be observed that $C_{11}H_x^+$ (green square) is only produced together with an acetylene ion, but that the acetylene ion can be produced with other monocations (blue rectangle). The TOF-TOF partial covariance map provides information on only three of the fragmentation channels involving dissociation of FLU^{2+} into $C_2H_x^+$ (with $C_{11}H_y^+$), $C_3H_x^+$ (with $C_{10}H_y^+$), and $C_4H_x^+$ (with $C_9H_x^+$), shown in the **Supplementary Material**. To summarize, the mass spectrum and the covariance analysis help us to identify a number of major fragmentation pathways of FLU molecules when subjected to Vis and XUV radiation. The time-dependent results are shown in the next section to understand the time evolution of the XUV-initiated dynamics in FLU molecules, probed using Vis photons.

3.2 Time-Resolved Results

3.2.1 Fragmentation Channels and Their Relative Intensities

We probed the dynamics and fragmentation pathways of fluorene initiated by the XUV photons at different delay times Δt using Vis photons. In the following, negative time delays ($\Delta t < 0$) denote Vis light irradiating the FLU molecules before the XUV pulse, and positive delays ($\Delta t > 0$) denote XUV pulses arriving earlier than Vis pulses, where the time at which the pulses coincide corresponds to $\Delta t = 0$. In the notation (i,j), "i" indicates the charge state of the ion of interest, and "j" depicts the charge state of the partner produced along with the ion of interest. The (1,0) channel would thus correspond to a monocation (ion of interest) recoiling against a neutral partner. Such products will have lower momentum than in the case of the (1,1) channel, where the monocation is recoiling against another monocation and experiences Coulomb repulsion, which is absent when recoiling against a neutral partner. We specify $C_2H_x^+$, $C_3H_x^+$, $C_4H_x^+$ as small fragments, $C_{10}H_x^+$ and $C_{11}H_x^+$ as large fragments, and the others are considered as medium fragments.

Figure 5A shows the delay-time averaged velocity-map ion images for two fragments $C_4H_x^+$ and $C_9H_y^+$. These images were processed to obtain the momentum distribution as a function of delay time shown in **Figure 5B**, which can be divided into three channels: (1,0), (1,1), and (1,2) to depict low, medium, and high momentum regions, respectively. The signal intensity is then integrated over the momentum coordinate to generate pump-probe delay time-dependent ion yields in these distinct channels (green points in **Figures 6C,D**).

FLU undergoes single and double ionization upon interaction with XUV photons, the resulting parent monocation and the dication interact with the Vis probe pulse and dissociate into the (1,0) and (1,1) channels of the fragment ions, respectively. This dissociation is evident by a sudden decrease in signal for the parent ions accompanied by an increase in the intensity of fragment ions after $\Delta t = 0$. For small fragments, the (1,1) channel is observed to be the most dominant amongst the (1,0), (1,1) and (1,2) channels as shown in **Figure 5B** for

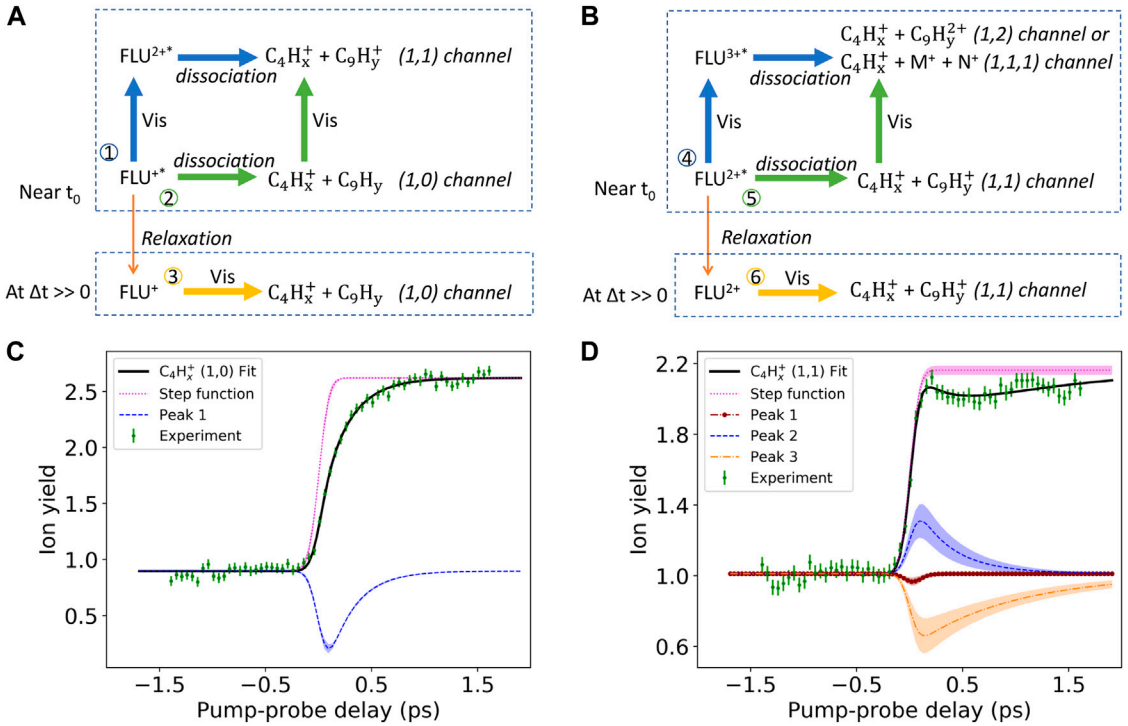

FIGURE 6 | Schematics of the XUV-pump, Vis-probe regime for the monocation and dication, **(A)** and **(B)**, respectively. The orange arrow depicts the relaxation of electronically excited ions over time. The letters M and N depict other possible fragments, which may be produced with the fragment $C_4H_x^+$. Ion yield dependences [in **(B)**] on the pump-probe delay time for the fragment ion $C_4H_x^+$ is shown for both (1,0) **(C)** and (1,1) channel **(D)**. The black curve is the final fitted curve, which is the result of transient peaks (blue, brown, and orange) and the step function (magenta curve). In all the curves the shaded area depicts the error. **(C)** The downward transient peak in the (1,0) channel depicts the transient depletion in the ion yield. **(D)** The (1,1) channel is fitted with three transient features, which comprises of two peaks showing transient decrease in the ion yields (peak 1 and peak 3) and one peak indicating transient increase (peak 2).

$C_4H_x^+$. On the contrary, the medium-sized fragments are observed to be mostly produced through the (1,0) channel, shown in **Figure 5B** for $C_9H_y^+$. The preference of the (1,0) channel and (1,1) channel by medium and small-sized ions, respectively, is explained as follows. During the dissociation of the parent monocation, the charge is mostly carried by the larger fragment than the smaller fragment due to higher ionization potential energy of the smaller fragment. As a result, the medium-sized fragments carry away the charges and are produced with neutrals in the (1,0) channel. The dissociation of the parent dication into the (1,1) channel is energetically favorable, which results in the production of small fragment ions in the (1,1) channel. Therefore, small charged ions are preferably produced with other medium-sized ions in the (1,1) channel than being produced in the (1,0) channel. Although the medium-sized ions are being produced through both channels (1,0) and (1,1), the (1,0) channel is observed to be more pronounced because of the larger production of the parent monocations as shown in **Figure 5B**. A similar trend in the preference of the channels is shown in the **Supplementary Material** for other small and medium-sized fragments.

3.2.2 Internal Relaxation Lifetimes

The experimental delay-time dependent ion yields are displayed with green points in **Figures 6C,D**. The black curve shows the final fit result, which has two major components, namely the step function (magenta curve) and transient peaks (blue, orange, and brown curves). The step function corresponds to the transition from the Vis-pump/XUV-probe (negative Δt) regime to the XUV-pump/Vis-probe (positive Δt) regime. The pronounced increase/decrease in the ion yields are depicted by transient peaks, which are observed in the positive Δt regions, i.e., we observed transient features when the FLU molecules are first pumped by the XUV photons to the singly and doubly ionized states, and the resulting parent monocations and dications dissociate through a number of fragmentation pathways after interaction with the Vis pulses. The various fragmentation channels arise from different ensembles of electronic states, giving rise to different relaxation lifetimes for each channel. In the following, we address the average electronic relaxation lifetimes of FLU monocation and dication obtained from the data on dissociation into $C_4H_x^+$ through the (1,0) and (1,1) channel. The $C_4H_x^+$ ion is highlighted as an example, which shows all the features observed across the other fragment ions.

FLU^{+*}: After absorbing an XUV photon, the FLU monocation may be formed in electronically excited states (FLU^{+*}), which relaxes over time to low-lying electronic states depicted as FLU^+. The relaxation process is probed using Vis pulses, as shown schematically in **Figure 6A**. Near t_0, FLU^{+*} may undergo two processes, denoted by pathways (1) and (2). The Vis pulse may

induce dissociative ionization, promoting $FLU^{+\star}$ to $FLU^{2+\star}$ that dissociates into $C_4H_x^+$ and $C_9H_y^+$ [the (1,1) channel of $C_4H_x^+$], demonstrated by pathway (1) following the blue arrows. As a side note, $C_4H_x^+$ could also be produced with other monocations in a (1,1,0) channel with neutral co-fragments. Another possibility is that $FLU^{+\star}$ can spontaneously dissociate through the (1,0) channel of $C_4H_x^+$ before the arrival of the probe pulse. The Vis pulse can ionize the neutral fragments produced in the (1,0) channel of $C_4H_x^+$ and convert the (1,0) channel to a (1,1) channel as indicated by pathway (2) following the green arrows. During this conversion, the two charged fragments in the resulting (1,1) channel are still close enough to face a strong Coulombic repulsion and must appear in the (1,1) channel region of the momentum distribution. Upon arrival of the Vis pulse during the evolution of the system along pathway (2), the (1,0) channel can in principle also lead to a (2,0) channel, if the Vis pulse ionizes the charged fragment ($C_4H_x^+$) rather than the neutral C_9H_y, thus there may also be a conversion from the (1,0) to the (2,0) channel. Since double ionization of the small fragment has a comparable low probability and we do not observe this conversion, this process is not discussed here and is not included in the schematic. At longer delay, the $FLU^{+\star}$ electronically relaxes (orange arrow in **Figure 6A**), and the Vis pulses can only lead to dissociation of relaxed FLU^+ through the (1,0) channel [pathway (3)].

Overall, these three pathways contribute to the transient increase in the (1,1) channel of $C_4H_x^+$ (blue peak 2 in **Figure 6D**), which matches the transient decrease in the (1,0) channel of the $C_4H_x^+$ yield (blue peak 1 in **Figure 6C**) near time $\Delta t = 0$. The timescales of the transient peaks correspond to the relaxation lifetime of the $FLU^{+\star}$ electronic states, which lead to the formation of $C_4H_x^+$ in the channels described above. These lifetimes are found to be 249 ± 10 fs and 339 ± 77 fs, for the depletion of the (1,0) [pathway (3)] and increase in the (1,1) channel (pathways (1) and (2) in **Figure 6A**, respectively). In addition to relaxation *via* carbon loss fragmentation channels, the H-loss channel also shows a transient increase, with a relaxation lifetime of 136 ± 7 fs. All other fragments have similar transient increase and decrease features in their (1,1) and (1,0) channels, respectively, except $C_2H_x^+$, where the data had a significant N_2^+ contamination. These are shown in the **Supplementary Material**.

$FLU^{2+\star}$: XUV photon absorption also forms FLU in an electronically excited dication state, $FLU^{2+\star}$. Similar to the processes described above, near t_0 we probe a number of dissociative pathways. Pathway (4) demonstrates dissociative ionization of $FLU^{2+\star}$ after interaction with Vis photons forming $FLU^{3+\star}$, which dissociates through either (1,2) or (1,1,1) channels (monocation recoiling against two other monocations), shown in **Figure 6B** following the blue arrows. The other pathway (5) depicts spontaneous dissociation of the $FLU^{2+\star}$ ions into the (1,1) channel, before the arrival of the Vis pulse. The Vis pulse may lead to the formation of the (1,2) or (1,1,1) channel of $C_4H_x^+$. If alternatively there is a sufficiently long delay time, the $FLU^{2+\star}$ molecules relax to FLU^{2+}, and promotion to the next ionization state by the Vis pulse is less favoured. The relaxed FLU^{2+} can then dissociate through the (1,1) channel upon arrival of the Vis pulse.

We observed two peaks depicting transient depletion in the ion yields in the (1,1) channel of $C_4H_x^+$, indicated as peak 1 (brown) and peak 3 (orange) in **Figure 6D**. The less intense peak 1 corresponds to a short lifetime of 30 ± 14 fs showing the depletion in the ion yield near t_0. This depletion is attributed to the corresponding transient increase in the (1,2) channel of $C_4H_x^+$. In our experiments, the signal for the (1,2) channel is very low, which could be due to the less intense probe pulse, and the corresponding increase in the (1,2) channel is not observed clearly. But the presence of the (1,2) channel for the fragment ion $C_3H_x^+$ was visible in a previous study with a different probe (810 nm), and a similar short lifetime of 17 ± 5 fs was reported [16]. Therefore, the peak 1 can be attributed to the shifting of population from the (1,1) channel to the (1,2) channel of $C_4H_x^+$ near t_0.

Peak 3 with a long lifetime of 1001 ± 204 fs can be attributed to the formation of the (1,1,1) channel. Formation of the (1,1,1) channel initiated by the Vis pulse involves production of three fragment ions, which can be produced at any time after the Vis pulse interaction. This leads to their production in a longer time span resulting in longer lifetime. The corresponding increase in the (1,1,1) channel can not be shown since this channel will have a large momentum distribution that could not be disentangled through the momentum maps. To summarize, the relaxation lifetime of $FLU^{2+\star}$ is determined *via* three pathways (4), (5), and (6), which result in transient depletion in the (1,1) channel resolvable for conversion into two dissociation channels, namely the (1,2) channel with a lifetime of 30 ± 14 fs and the (1,1,1) channel with a lifetime of 1001 ± 204 fs.

In addition to the $FLU^{2+\star}$ lifetimes obtained through the carbon skeleton fragmentation channels, we also obtained the relaxation lifetime of the FLU dication dissociating through the H-loss channel, which was found to be 117 ± 6 fs. The H-loss relaxation lifetimes of $FLU^{2+\star}$ and $FLU^{+\star}$ are similar and indicate that hydrogen loss from the parent ion, which involves σ-bond fission, is unaffected by the difference in the charge states that are mostly localized in the conjugated-π system. The lifetimes extracted from other fragments are tabulated in the **Supplementary Material**.

The fragment ions with higher masses than $C_6H_x^+$ were fitted with a single transient increase peak. The absence of multiple peaks in the (1,1) channels for these heavier mass fragments is attributed to the following two reasons. Firstly, the conversion from the (1,1) channel to the (1,2) channel for the higher masses might be inaccessible since the small partner ions of these large fragments are difficult to doubly ionize by the Vis pulse, due to the higher ionization potential compared to the larger fragments and even higher double ionization potential. Secondly, the (1,1,1) channel is formed by the dissociation of the FLU trication into smaller fragments, and hence this channel is likely to have a significantly smaller branching ratio due to the fact that one of the fragments is already large.

Relaxation lifetimes for near-ionization-threshold electronic states of $FLU^{2+\star}$ could also be extracted from the transient increase in the FLU trication signal. As depicted in process (4) in the schematic of **Figure 6B**, the Vis pulse absorption by $FLU^{2+\star}$ results in the formation of FLU trication, observed as a transient increase in the FLU^{3+} ion yield. This transient peak corresponds to a relaxation lifetime of 184 ± 44 fs, which was measured using 405 nm Vis photons as the probe pulse (~390 μJ pulse energy).

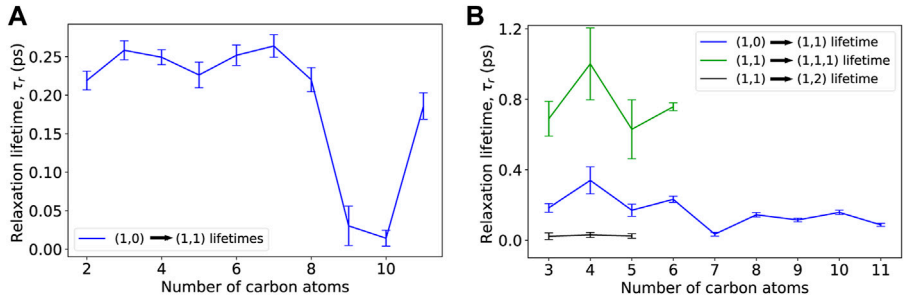

FIGURE 7 | Observed trends as a function of fragment size. **(A)** Relaxation lifetime of $FLU^{+\star}$ plotted as a function of the number of carbon atoms of the fragment, with which the relaxation lifetime is associated. This demonstrates the depletion of the (1,0) channel and the formation of the (1,1) channel. **(B)** Relaxation lifetime of FLU monocation and dication plotted as a function of the number of carbon atoms of the fragment obtained from the (1,1) channel, depicting three processes. First, conversion of the (1,0) channel to the (1,1) channel, which corresponds to the electronic relaxation lifetimes of the FLU monocation (blue curve). Second, conversion of the (1,1) channel to the (1,2) channel, which corresponds to the electronic relaxation lifetimes of the FLU dication (black curve). Third, conversion of the (1,1) channel to the (1,1,1) channel, which also corresponds to the electronic relaxation lifetimes of the FLU dication (green curve). The fragment ion $C_2H_x^+$ with a lifetime of 2.987 ± 0.006 ps, which would be on the blue curve, has been omitted for better visibility of the other fragments with much shorter lifetimes.

The relaxation lifetime was also determined before using XUV-IR (30.3 and 810 nm) [16] pump-probe studies to be 126 ± 16 fs, which is somewhat lower compared to the XUV-Vis studies reported here.

4 DISCUSSION

4.1 Effect of Fragment Size on the Observed Relaxation Lifetimes

The relaxation of the electronically excited FLU monocation and dication is probed *via* Vis pulses by inducing dissociation and/or dissociative ionization. Various fragment ions thus produced would show different relaxation lifetimes (τ_r) of FLU^+ and FLU^{2+}. The effect of the fragment ion's size on the τ_r can be observed in **Figures 7A,B**, where we plot the identified relaxation lifetimes as a function of the number of carbon atoms in the fragment ion. The respective τ_r of $FLU^{+\star}$ determined through the (1,0) channel and the (1,1) channel are depicted by the blue curves in **Figures 7A,B**. The small fragments with number of carbons atoms from two to eight indicate similar lifetimes (τ_r) whereas the large fragments $C_9H_x^+$ and $C_{10}H_x^+$ except $C_{11}H_x^+$ show longer τ_r.

The longer and shorter relaxation lifetimes for the small and large fragments, respectively, can be explained as follows: as can be inferred from the covariance maps (**Figure 4**), the smaller fragments have more possible dissociation partners, and hence more fragmentation pathways are associated with them. The relaxation of $FLU^{+\star}$ into these multiple pathways, involving the formation of a small fragment with various other partners, is not completely resolvable. The resultant transient peaks thus have contributions from all possible formation pathways, and hence longer lifetimes are observed compared to the large fragments having a relatively low number of formation pathways resulting in shorter lifetimes.

The longer lifetime corresponding to the $C_{11}H_x^+$ fragment ion is an exception to the lifetimes extracted from other large fragment ions. This exception is attributed to the fact that the formation pathway of $C_{11}H_x^+$ involves acetylene loss from the parent species. This pathway is thought to progress *via* a mechanism involving rearrangement of the rings to allow C_2H_2 loss described in Ref. [67], which is not the case for the C_3H_x loss or C_4H_x loss leading to the formation of other large fragments. This low-energy dissociative pathway forming $C_{11}H_x^+$ is likely to be initiated by the Vis pulse from a wide range of electronic states of FLU^+, which results in longer relaxation lifetimes. The relaxation lifetimes of $FLU^{2+\star}$ were obtained from the shift of population from the (1,1) channel to the (1,2) and (1,1,1) channels of small fragment ions. The absence of these features in the large fragments was explained in the previous section. The observation of similar lifetimes for small fragments is consistent here as depicted by the green and black curve in **Figure 7B**.

4.2 Effect of Probe Pulse on the Observed Relaxation Lifetimes

As reported in the results section, the relaxation lifetimes of $FLU^{2+\star}$ were found to be different when probed with IR and Vis pulses. This difference in the recorded lifetime with the Vis pulse is attributed to its higher probe energy, which is able to excite lower-lying states of $FLU^{2+\star}$ to $FLU^{3+\star}$, resulting in an increase in the observed relaxation lifetimes.

5 SUMMARY AND CONCLUSION

We studied the interaction of FLU molecules with XUV radiation, which is present in the interstellar medium as He II emission line. FLU was observed to undergo numerous processes, involving single and double ionization, dominant single dehydrogenation post single ionization, and fragmentation into various carbon loss channels with acetylene loss being a major process. The fragments observed in the mass spectrum can be thought of as potential ions that would be present in the ISM as a result of UV induced photodissociation.

The recoil-frame covariance technique exhibited the primary, secondary, and tertiary fragmentation of the parent dication that have occurred from a high amount of residual energy given by the high-energy photons. The ultrafast pump-probe measurements with the 405 nm probe enabled us to investigate the ultrafast decay of electronically excited and highly energetic parent ions that are promoted to the next charge state dissociation and/or non-dissociation channels.

Interaction with high energy photons opened the possibility for parent ion dissociation through a large number of fragmentation pathways. The momentum resolution provided by the velocity map imaging made it possible to distinguish between several channels for the fragments, which we label as (1,0), (1,1) and (1,2) channels. A detailed analysis on the fragments showed the transient depletion and enhancement of the ion yields, as a result of the $FLU^{+\star}$ and $FLU^{2+\star}$ ions' temporal relaxation into different energy levels. It is interesting to observe the time-resolved shift of the population from one channel to another one of the observed fragments, revealing the lifetimes of the species they are formed from. The results enabled us to determine the dependence of the relaxation lifetimes on the fragment size. These relaxation lifetimes were reported to be in the range of 10 fs to a few ps. The range of the lifetimes is similar to the lifetimes that were reported to be in the range of 10–100 fs using XUV-IR pump-probe spectroscopy [16, 18, 26].

In this work, we used and discussed different experimental and analytical tools to investigate the fundamental photophysics and chemical processes engaged after the interaction of fluorene with XUV radiation. Through these processes, the relaxation lifetimes of the fluorene parent ions were extracted, which are beneficial to gaining a complete view of the timescales of small PAHs. All dissociation products from fluorene were found to have reaction pathways decaying on the sub-picosecond timescale, indicating non-adiabatic relaxation mediated by a high number of conical intersections. As PAHs typically have a high density of states, similar to fluorene, ultrafast relaxation across all charge states investigated might be expected amongst PAH molecules in general. Overall, exploring the possible reaction pathways of the fluorene cations in its non-radiative regime is advantageous for the fundamental femtochemistry and astrochemistry fields.

DATA AVAILABILITY STATEMENT

The original contributions presented in the study are included in the article/**Supplementary Material**, further inquiries can be directed to the corresponding author.

AUTHOR CONTRIBUTIONS

BM and MS conceived and designed the experiments. JWLL, PC, SM, AS, SG, FA, RB, XC, SD, BE, LH, DH, MJ, MK, HK, JL, AL, DL, RM, EM, TM, PO, CP, JP, DRa, DRom, STr, JW, FZ, SB, MBu, DRol, STe, PJ, BM, and MS performed the experiments. DG, JWLL, DT, PC, SM, AS, SG, and EM analyzed the data. DG, JWLL, DT, PC, AS, BE, FA, MBu, JK, AR, DRol, RB, PJ, MBr, CV, BM, and MS performed detailed discussions of the results. DG, JWLL, DT, and MS wrote the manuscript.

FUNDING

This work was supported by the ERC Starting Grant ASTROROT, grant number 638027, and the project CALIPSOplus under the grant agreement 730872 from the EU Framework Programme for Research and Innovation HORIZON 2020. The experimental parts of this research were carried out at beamline BL1 FLASH at DESY, a member of the Helmholtz Association (HGF). Beamtime was allocated for proposal F-20170540. We acknowledge the Max Planck Society for funding the development and the initial operation of the CAMP end-station within the Max Planck Advanced Study Group at CFEL and for providing this equipment for CAMP@FLASH. The installation of CAMP@FLASH was partially funded by the BMBF grants 05K10KT2, 05K13KT2, 05K16KT3, and 05K10KTB from FSP-302. We acknowledge financial support by the European Union's Horizon 2020 research and innovation program under the Marie Skłodowska-Curie Grant Agreement 641789 "Molecular Electron Dynamics investigated by Intense Fields and Attosecond Pulses" (MEDEA), the Clusters of Excellence "Center for Ultrafast Imaging" (CUI, EXC 1074, ID 194651731), the "Advanced Imaging of Matter" (AIM, EXC 2056, ID 390715994) of the Deutsche Forschungsgemeinschaft (DFG), the European Research Council under the European Union's Seventh Framework Programme (FP7/2007–2013) through the Consolidator Grant COMOTION (614507), and the Helmholtz Gemeinschaft through the "Impuls- und Vernetzungsfonds". In addition, the project was supported by The Netherlands Organization for Scientific Research (NWO) and is part of the Dutch Astrochemistry Network (DAN) II (Project No. 648.000.029). PE-J, SM, and JP acknowledge support from the Swedish Research Council and the Swedish Foundation for Strategic Research. The authors are additionally thankful for the support from the following funding bodies: the UK EPSRC (MBR and CV-EP/L005913/1 and EP/V026690/1; MBU-EP/S028617/1), STFC (PNPAS award and mini-IPS Grant No. ST/J002895/1), the Chemical Sciences, Geosciences, and Biosciences Division, Office of Basic Energy Sciences, Office of Science, US Department of Energy (FZ—DE-FG02-86ER13491); the National Science Foundation (DR - PHYS-1753324); and the Helmholtz Initiative and Networking Fund through the Young Investigators Group Program (SB). We acknowledge the use of the Maxwell computational resources operated at Deutsches Elektronen-Synchrotron DESY, Hamburg, Germany.

SUPPLEMENTARY MATERIAL

The Supplementary Material for this article can be found online at: https://www.frontiersin.org/articles/10.3389/fphy.2022.880793/full#supplementary-material

REFERENCES

1. Ehrenfreund P, Sephton MA. Carbon Molecules in Space: from Astrochemistry to Astrobiology. *Faraday Discuss* (2006) 133:277. doi:10.1039/b517676j
2. Herbst E, van Dishoeck EF. Complex Organic Interstellar Molecules. *Annu Rev Astron Astrophys* (2009) 47:427–80. doi:10.1146/annurev-astro-082708-101654
3. Tielens AGGM. Interstellar Polycyclic Aromatic Hydrocarbon Molecules. *Annu Rev Astron Astrophys* (2008) 46:289–337. doi:10.1146/annurev.astro.46.060407.145211
4. Ziurys LM. The Chemistry in Circumstellar Envelopes of Evolved Stars: Following the Origin of the Elements to the Origin of Life. *Proc Natl Acad Sci U.S.A* (2006) 103:12274–9. doi:10.1073/pnas.0602277103
5. Tielens AGGM. The Aromatic Universe. In: *Molecular Astrophysics*. Cambridge: Cambridge University Press (2021). p. 567–628. doi:10.1017/9781316718490.013
6. Allamandola LJ, Tielens AGGM, Barker JR. Interstellar Polycyclic Aromatic Hydrocarbons: The Infrared Emission Bands, the Excitation/Emission Mechanism, and the Astrophysical Implications. *Astrophysical J Suppl Ser* (1989) 71:733. doi:10.1086/191396
7. Berné O, Joblin C, Rapacioli M, Thomas J, Cuillandre J-C, Deville Y. Extended Red Emission and the Evolution of Carbonaceous Nanograins in NGC 7023. *Astron Astrophysics* (2008) 479:L41–L44. doi:10.1051/0004-6361:20079158
8. Rapacioli M, Joblin C, Boissel P. Spectroscopy of Polycyclic Aromatic Hydrocarbons and Very Small Grains in Photodissociation Regions. *Astron Astrophysics* (2004) 429:193–204. doi:10.1051/0004-6361:20041247
9. Peeters E, Hony S, Van Kerckhoven C, Tielens AGGM, Allamandola LJ, Hudgins DM, et al. The Rich 6 to 9 $\vec\μ$m Spectrum of Interstellar PAHs. *Astron Astrophysics* (2002) 390:1089–113. doi:10.1051/0004-6361:20020773
10. Cernicharo J, Agúndez M, Cabezas C, Tercero B, Marcelino N, Pardo JR, et al. Pure Hydrocarbon Cycles in TMC-1: Discovery of Ethynyl Cyclopropenylidene, Cyclopentadiene, and Indene. *Astron Astrophysics* (2021) 649:L15. doi:10.1051/0004-6361/202141156
11. Burkhardt AM, Long Kelvin Lee K, Bryan Changala P, Shingledecker CN, Cooke IR, Loomis RA, et al. Discovery of the Pure Polycyclic Aromatic Hydrocarbon Indene (c-C9H8) with GOTHAM Observations of TMC-1. *ApJL* (2021) 913:L18. doi:10.3847/2041-8213/abfd3a
12. McGuire BA, Loomis RA, Burkhardt AM, Lee KLK, Shingledecker CN, Charnley SB, et al. Detection of Two Interstellar Polycyclic Aromatic Hydrocarbons via Spectral Matched Filtering. *Science* (2021) 371:1265–9. doi:10.1126/science.abb7535
13. Doddipatla S, Galimova GR, Wei H, Thomas AM, He C, Yang Z, et al. Low-temperature Gas-phase Formation of Indene in the Interstellar Medium. *Sci Adv* (2021) 7:4044. doi:10.1126/sciadv.abd4044
14. Kaiser RI, Parker DSN, Mebel AM. Reaction Dynamics in Astrochemistry: Low-Temperature Pathways to Polycyclic Aromatic Hydrocarbons in the Interstellar Medium. *Annu Rev Phys Chem* (2015) 66:43–67. doi:10.1146/annurev-physchem-040214-121502
15. Campbell EK, Holz M, Gerlich D, Maier JP. Laboratory Confirmation of C_{60}^+ as the Carrier of Two Diffuse Interstellar Bands. *Nature* (2015) 523:322–3. doi:10.1038/nature14566
16. Lee JWL, Tikhonov DS, Chopra P, Maclot S, Steber AL, Gruet S, et al. Time-resolved Relaxation and Fragmentation of Polycyclic Aromatic Hydrocarbons Investigated in the Ultrafast XUV-IR Regime. *Nat Commun* (2021) 12:6107. doi:10.1038/s41467-021-26193-z
17. Robson L, Tasker AD, Ledingham KWD, McKenna P, McCanny T, Kosmidis C, et al. Ionisation and Fragmentation Dynamics of Laser Desorbed Polycyclic Aromatic Hydrocarbons Using Femtosecond and Nanosecond post-ionisation. *Int J Mass Spectrom* (2002) 220:69–85. doi:10.1016/s1387-3806(02)00823-0
18. Marciniak A, Despré V, Barillot T, Rouzée A, Galbraith MCE, Klei J, et al. XUV Excitation Followed by Ultrafast Non-adiabatic Relaxation in PAH Molecules as a Femto-Astrochemistry experiment. *Nat Commun* (2015) 6:8909. doi:10.1038/ncomms8909
19. Bagdia C, Biswas S, Mandal A, Bhattacharjee S, Tribedi LC. Ionization and Fragmentation of Fluorene upon 250 keV Proton Impact. *Eur Phys J D* (2021) 75:37. doi:10.1140/epjd/s10053-020-00001-7
20. Zhen J, Castillo SR, Joblin C, Mulas G, Sabbah H, Giuliani A, et al. Vuv Photo-Processing of PAH Cations: Quantitative Study on the Ionization versus Fragmentation Processes. *Astrophysical J* (2016) 822:113. doi:10.3847/0004-637x/822/2/113
21. Bazzi S, Welsch R, Vendrell O, Santra R. Challenges in XUV Photochemistry Simulations: A Case Study on Ultrafast Fragmentation Dynamics of the Benzene Radical Cation. *J Phys Chem A* (2018) 122:1004–10. doi:10.1021/acs.jpca.7b11543
22. Reddy VS, Ghanta S, Mahapatra S. First Principles Quantum Dynamical Investigation Provides Evidence for the Role of Polycyclic Aromatic Hydrocarbon Radical Cations in Interstellar Physics. *Phys Rev Lett* (2010) 104:111102. doi:10.1103/physrevlett.104.111102
23. Domcke W, Yarkony DR. Role of Conical Intersections in Molecular Spectroscopy and Photoinduced Chemical Dynamics. *Annu Rev Phys Chem* (2012) 63:325–52. doi:10.1146/annurev-physchem-032210-103522
24. Galbraith MCE, Scheit S, Golubev NV, Reitsma G, Zhavoronkov N, Despré V, et al. Few-femtosecond Passage of Conical Intersections in the Benzene Cation. *Nat Commun* (2017) 8:1018. doi:10.1038/s41467-017-01133-y
25. Curchod BFE, Martínez TJ. Ab Initio nonadiabatic Quantum Molecular Dynamics. *Chem Rev* (2018) 118:3305–36. doi:10.1021/acs.chemrev.7b00423
26. Hervé M, Despré V, Castellanos Nash P, Loriot V, Boyer A, Scognamiglio A, et al. Ultrafast Dynamics of Correlation Bands Following XUV Molecular Photoionization. *Nat Phys* (2020) 17:327–31. doi:10.1038/s41567-020-01073-3
27. Bernstein MP, Sandford SA, Allamandola LJ, Gillette JS, Clemett SJ, Zare RN. UV Irradiation of Polycyclic Aromatic Hydrocarbons in Ices: Production of Alcohols, Quinones, and Ethers. *Science* (1999) 283:1135–8. doi:10.1126/science.283.5405.1135
28. Boyer A, Hervé M, Despré V, Castellanos Nash P, Loriot V, Marciniak A, et al. Ultrafast Vibrational Relaxation Dynamics in XUV-Excited Polycyclic Aromatic Hydrocarbon Molecules. *Phys Rev X* (2021) 11:041012. doi:10.1103/physrevx.11.041012
29. Bouwman J, Cuppen HM, Steglich M, Allamandola LJ, Linnartz H. Photochemistry of Polycyclic Aromatic Hydrocarbons in Cosmic Water Ice. *Astron Astrophysics* (2011) 529:A46. doi:10.1051/0004-6361/201015762
30. Ruehl E, Price SD, Leach S. Single and Double Photoionization Processes in Naphthalene between 8 and 35 eV. *J Phys Chem* (1989) 93:6312–21. doi:10.1021/j100354a011
31. Leach S, Eland JHD, Price SD. Formation and Dissociation of Dications of Naphthalene-D8. *J Phys Chem* (1989) 93:7583–93. doi:10.1021/j100359a014
32. Lu J, Ren X, Cao L. Studies on Characteristics and Formation of Soot Nanoparticles in an Ethylene/air Inverse Diffusion Flame. *J Energ Eng.* (2016) 142:04015041. doi:10.1061/(asce)ey.1943-7897.0000305
33. Petrignani A, Vala M, Eyler JR, Tielens AGGM, Berden G, van der Meer AFG, et al. Breakdown Products of Gaseous Polycyclic Aromatic Hydrocarbons Investigated with Infrared Ion Spectroscopy. *Astrophysical J* (2016) 826:33. doi:10.3847/0004-637x/826/1/33
34. Güsten H, Klasinc L, Marsel J, Milivojević D. A Comparative Study of the Mass Spectra of Stilbene and Fluorene. *Org Mass Spectrom* (1972) 6:175–8. doi:10.1002/oms.1210060207
35. Bowie JH, Bradshaw TK. Electron Impact Studies. LVI. The Fluorenyl and Phenalenyl Cations. the Application of Metastable Characteristics. *Aust J Chem* (1970) 23:1431. doi:10.1071/ch9701431
36. Zhang W, Si Y, Zhen J, Chen T, Linnartz H, Tielens AGGM. Laboratory Photochemistry of Covalently Bonded Fluorene Clusters: Observation of an Interesting PAH Bowl-Forming Mechanism. *Astrophysical J* (2019) 872:38. doi:10.3847/1538-4357/aafe10
37. Andrews H, Boersma C, Werner MW, Livingston J, Allamandola LJ, Tielens AGGM. PAH Emission at the Bright Locations of PDRs: The grandPAH Hypothesis. *Astrophysical J* (2015) 807:99. doi:10.1088/0004-637x/807/1/99
38. Ackermann W, Asova G, Ayvazyan V, Azima A, Baboi N, Bähr J, et al. Operation of a Free-Electron Laser from the Extreme Ultraviolet to the Water Window. *Nat Photon* (2007) 1:336–42. doi:10.1038/nphoton.2007.76
39. Erk B, Müller JP, Bomme C, Boll R, Brenner G, Chapman HN, et al. CAMP@FLASH: an End-Station for Imaging, Electron- and Ion-Spectroscopy, and

Pump-Probe Experiments at the FLASH Free-Electron Laser. *J Synchrotron Radiat* (2018) 25:1529–40. doi:10.1107/s1600577518008585
40. Düsterer S, Rehders M, Al-Shemmary A, Behrens C, Brenner G, Brovko O, et al. Development of Experimental Techniques for the Characterization of Ultrashort Photon Pulses of Extreme Ultraviolet Free-Electron Lasers. *Phys Rev ST Accel Beams* (2014) 17:120702. doi:10.1103/physrevstab.17.120702
41. Behrens C, Gerasimova N, Gerth C, Schmidt B, Schneidmiller EA, Serkez S, et al. Constraints on Photon Pulse Duration from Longitudinal Electron Beam Diagnostics at a Soft X-ray Free-Electron Laser. *Phys Rev ST Accel Beams* (2012) 15:030707. doi:10.1103/physrevstab.15.030707
42. Redlin H, Al-Shemmary A, Azima A, Stojanovic N, Tavella F, Will I, et al. The FLASH Pump-Probe Laser System: Setup, Characterization and Optical Beamlines. *Nucl Instr Methods Phys Res Section A: Acc Spectrometers, Detectors Associated Equipment* (2011) 635:S88–S93. doi:10.1016/j.nima.2010.09.159
43. Eppink ATJB, Parker DH. Velocity Map Imaging of Ions and Electrons Using Electrostatic Lenses: Application in Photoelectron and Photofragment Ion Imaging of Molecular Oxygen. *Rev Scientific Instr* (1997) 68:3477–84. doi:10.1063/1.1148310
44. Parker DH, Eppink ATJB. Photoelectron and Photofragment Velocity Map Imaging of State-Selected Molecular Oxygen Dissociation/ionization Dynamics. *J Chem Phys* (1997) 107:2357–62. doi:10.1063/1.474624
45. Even U. "The Even-Lavie Valve as a Source for High Intensity Supersonic Beam". *EPJ Techn Instrum* (2015) 2:17. doi:10.1140/epjti/s40485-015-0027-5
46. Clark AT, Crooks JP, Sedgwick I, Turchetta R, Lee JWL, John JJ, et al. Multimass Velocity-Map Imaging with the Pixel Imaging Mass Spectrometry (PImMS) Sensor: An Ultra-fast Event-Triggered Camera for Particle Imaging. *J Phys Chem A* (2012) 116:10897–903. doi:10.1021/jp309860t
47. Amini K, Blake S, Brouard M, Burt MB, Halford E, Lauer A, et al. Three-dimensional Imaging of Carbonyl Sulfide and Ethyl Iodide Photodissociation Using the Pixel Imaging Mass Spectrometry Camera. *Rev Scientific Instr* (2015) 86:103113. doi:10.1063/1.4934544
48. Jaycen A. Open-source Software Compares Abel Transforms for Easy Use. *Scilight* (2019) 2019:260003. doi:10.1063/1.5111853
49. Van Rossum G, Drake FL, Jr. *Python Reference Manual*. Amsterdam, Netherlands: Centrum voor Wiskunde en Informatica Amsterdam (1995).
50. Dahl DA, Delmore JE, Appelhans AD. SIMION PC/PS2 Electrostatic Lens Design Program. *Rev Scientific Instr* (1990) 61:607–9. doi:10.1063/1.1141932
51. [Dataset] Tikhonov DS. *MCMCMCFitting* (2019). Available from: https://stash.desy.de/projects/cfa/repos/mcmcmcfitting/browse (Accessed February 1, 2022).
52. [Dataset] Steber A, Müller E. *PAH* (2016). Available from: https://stash.desy.de/projects/cs/repos/pah/browse (Accessed February 1, 2022).
53. [Dataset] Tikhonov DS. *Campfancyanalysis* (2019). Available from: https://stash.desy.de/projects/cfa/repos/campfancyanalysis/browse (Accessed February 1, 2022).
54. Pedersen S, Zewail A. Femtosecond Real-Time Probing of Reactions XXII. Kinetic Description of Probe Absorption, Fluorescence, Depletion and Mass Spectrometry. *Mol Phys* (1996) 89:1455–502. doi:10.1080/002689796173291
55. Tikhonov DS. *CAMPFancyAnalyis Home* (2019). Available from: https://confluence.desy.de/display/CFA/CAMPFancyAnalyis+Home (Accessed February 1, 2022).
56. Savelyev E, Boll R, Bomme C, Schirmel N, Redlin H, Erk B, et al. Jitter-correction for IR/UV-XUV Pump-Probe Experiments at the FLASH Free-Electron Laser. *New J Phys* (2017) 19:043009. doi:10.1088/1367-2630/aa652d
57. Schulz S, Grguraš I, Behrens C, Bromberger H, Costello JT, Czwalinna MK, et al. Femtosecond All-Optical Synchronization of an X-ray Free-Electron Laser. *Nat Commun* (2015) 6:6938. doi:10.1038/ncomms6938
58. Frasinski LJ, Codling K, Hatherly PA. Covariance Mapping: A Correlation Method Applied to Multiphoton Multiple Ionization. *Science* (1989) 246:1029–31. doi:10.1126/science.246.4933.1029
59. Tikhonov DS. *TOF-TOF Covariance Analysis* (2019). Available from: https://confluence.desy.de/display/CFA/TOF-TOF+covariance+analysis (Accessed February 1, 2022).
60. Dabestani R, Ivanov IN. A Compilation of Physical, Spectroscopic and Photophysical Properties of Polycyclic Aromatic Hydrocarbons. *Photochem Photobiol* (1999) 70:10–34. doi:10.1111/j.1751-1097.1999.tb01945.x
61. Holm AIS, Johansson HAB, Cederquist H, Zettergren H. Dissociation and Multiple Ionization Energies for Five Polycyclic Aromatic Hydrocarbon Molecules. *J Chem Phys* (2011) 134:044301. doi:10.1063/1.3541252
62. Vinitha MV, Nair AM, Ramanathan K, Kadhane UR. Understanding Dehydrogenation Sequence in Fluorene$^+$ by Multiphoton Ionisation-Excitation Processes. *Int J Mass Spectrom* (2022) 471:116704. doi:10.1016/j.ijms.2021.116704
63. Frasinski LJ. Covariance Mapping Techniques. *J Phys B: Mol Opt Phys* (2016) 49:152004. doi:10.1088/0953-4075/49/15/152004
64. Slater CS, Blake S, Brouard M, Lauer A, Vallance C, John JJ, et al. Covariance Imaging Experiments Using a Pixel-Imaging Mass-Spectrometry Camera. *Phys Rev A* (2014) 89:011401. doi:10.1103/physreva.89.011401
65. Slater CS, Blake S, Brouard M, Lauer A, Vallance C, Bohun CS, et al. Coulomb-explosion Imaging Using a Pixel-Imaging Mass-Spectrometry Camera. *Phys Rev A* (2015) 91:053424. doi:10.1103/physreva.91.053424
66. Vallance C, Heathcote D, Lee JWL. Covariance-map Imaging: A Powerful Tool for Chemical Dynamics Studies. *J Phys Chem A* (2021) 125:1117–33. doi:10.1021/acs.jpca.0c10038
67. West BJ, Lesniak L, Mayer PM. Why Do Large Ionized Polycyclic Aromatic Hydrocarbons Not Lose C_2H_2? *J Phys Chem A* (2019) 123:3569–74. doi:10.1021/acs.jpca.9b01879

Conflict of Interest: The authors declare that the research was conducted in the absence of any commercial or financial relationships that could be construed as a potential conflict of interest.

Publisher's Note: All claims expressed in this article are solely those of the authors and do not necessarily represent those of their affiliated organizations, or those of the publisher, the editors and the reviewers. Any product that may be evaluated in this article, or claim that may be made by its manufacturer, is not guaranteed or endorsed by the publisher.